nature physics

LETTERS

PUBLISHED ONLINE: 10 OCTOBER 2016 | DOI: 10.1038/NPHYS3911

Nonergodic diffusion of single atoms in a periodic potential

Farina Kindermann[1], Andreas Dechant[2,3], Michael Hohmann[1], Tobias Lausch[1], Daniel Mayer[1,4], Felix Schmidt[1,4], Eric Lutz[2] and Artur Widera[1,4]*

Diffusion can be used to infer the microscopic features of a system from the observation of its macroscopic dynamics. Brownian motion accurately describes many diffusive systems, but non-Brownian and nonergodic features are often observed on short timescales. Here, we trap a single ultracold caesium atom in a periodic potential and measure its diffusion[1–3]. We engineer the particle–environment interaction to fully control motion over a broad range of diffusion constants and timescales. We use a powerful stroboscopic imaging method to detect single-particle trajectories and analyse both non-equilibrium diffusion properties and the approach to ergodicity[4]. Whereas the variance and two-time correlation function exhibit apparent Brownian motion at all times, higher-order correlations reveal strong non-Brownian behaviour. We additionally observe the slow convergence of the exponential displacement distribution to a Gaussian and—unexpectedly—a much slower approach to ergodicity[5], in perfect agreement with an analytical continuous-time random-walk model[6–8]. Our experimental system offers an ideal testbed for the detailed investigation of complex diffusion processes.

The concept of diffusion is ubiquitous in physics[9], chemistry[10] and biology[11]. Recent developments have lead to a better understanding of the diffusive behaviour of increasingly complex structures, from colloid particles[12] and anisotropic ellipsoids[13] to extended stiff filaments[14] and fluidized matter[15]. At the same time, the diffusion of tracer particles has become a powerful experimental tool to probe the properties of complex systems from turbulent fluids[16] to living cells[17].

In many systems, diffusion is well described by the theory of Brownian motion[1]. The hallmarks of standard Brownian diffusion are: a linear mean-square displacement (MSD), $\sigma^2(t) = \langle \Delta x_t^2 \rangle - \langle \Delta x_t \rangle^2 \propto 2Dt$, where D is the diffusion coefficient and $\langle \cdot \rangle$ denotes the average over many trajectories; a Gaussian displacement probability distribution, a direct consequence of the central-limit theorem; and ergodic behaviour in a potential, implying that ensemble and time averages are equal in the long-time limit. Ergodicity lies at the core of statistical mechanics and indicates that a single trajectory is representative for the ensemble[4]. However, an increasing number of systems exhibit nonergodic features owing to slow, non-exponential relaxation. Examples include blinking quantum dots[18], the motion of lipid granules[19], and mRNA molecules[20] and receptors in living cells[21]. These systems lie outside the range of standard statistical physics and their description is hence particularly challenging[5,22]. Of special interest is the question of the approach to ergodicity. Many relevant processes in nature indeed occur on finite timescales[19–21] during which ergodic behaviour cannot be taken for granted.

We experimentally realize an ideal system consisting of a single atom moving in a periodic potential and interacting with a near-resonant light field that acts as a thermal bath. Diffusion in a periodic potential is a paradigmatic model that has been extensively used to describe a variety of problems[1], from superionic conductors[2] and Josephson junctions[3] to phase-locked loops[23] and diffusion on surfaces[24]. We perfectly control all internal and external atomic degrees of freedom, as well as the properties of the light field and of the periodic potential. Therefore, we can tune and explore diffusion over a large range of parameters. Moreover, we stroboscopically image the motion of the single atoms and record their individual trajectories, a prerequisite for the investigation of ergodicity. The diffusion of large ensembles of atoms[25,26], as well as of single atoms in periodic potentials, has been examined in the past, but only ensemble properties have been determined[27]. The unique ability to monitor individual diffusive atoms allows us to compare the convergence of the displacement distribution to a Gaussian, as required by the central-limit theorem, and the approach to ergodicity. We demonstrate that ergodicity, quantified by the ergodicity breaking parameter (EBP), equation (7) (ref. 28), is established at a much slower pace than Gaussianity, characterized by the excess kurtosis, equation (6) (ref. 1). We further show that the MSD and the two-time position correlation function are identical to those of Brownian motion, at all times, and that a four-time correlation function is needed to identify non-Brownian features. Owing to its great tunability, our system offers a versatile platform to investigate in detail the effects of noise and disorder, as well as the influence of confinement and of external forces on general diffusion phenomena.

We initialize the system by preparing a single laser-cooled caesium (Cs) atom, thermalized with a laser light field at a temperature of $T_0 \approx 50\,\mu$K. We trap the particle in a periodic potential of a one-dimensional optical lattice with depth $U_0 = k_B \times 850\,\mu$K and lattice spacing $\lambda/2 = 395$ nm, where no dynamics is observed. Here k_B is the Boltzmann constant and λ the wavelength of the lattice laser light. Along the lattice axis, the atom is trapped in the nodes of the interference light field. Transversely, the atom is confined by a 1,064 nm running wave dipole trap, spatially overlapped with the lattice axis. The dipole trap also contributes a harmonic confinement along the lattice axis with trapping frequency $\omega \approx 2\pi \times 60$ Hz for atoms leaving the lattice potential. The atom is hence initially confined to disc-shaped lattice wells and performs rapid in-well dynamics. Diffusion along the lattice axis is generated by, first, adiabatically lowering the depth to $U_{low} = k_B \times 210\,\mu$K, enabling the

[1]Department of Physics and Research Center OPTIMAS, University of Kaiserslautern, 67663 Kaiserslautern, Germany. [2]Department of Physics, Friedrich-Alexander-Universität Erlangen-Nürnberg, 91058 Erlangen, Germany. [3]Department of Physics, Kyoto University, 606-8502 Kyoto, Japan. [4]Graduate School Materials Science in Mainz, 67663 Kaiserslautern, Germany. *e-mail: widera@physik.uni-kl.de

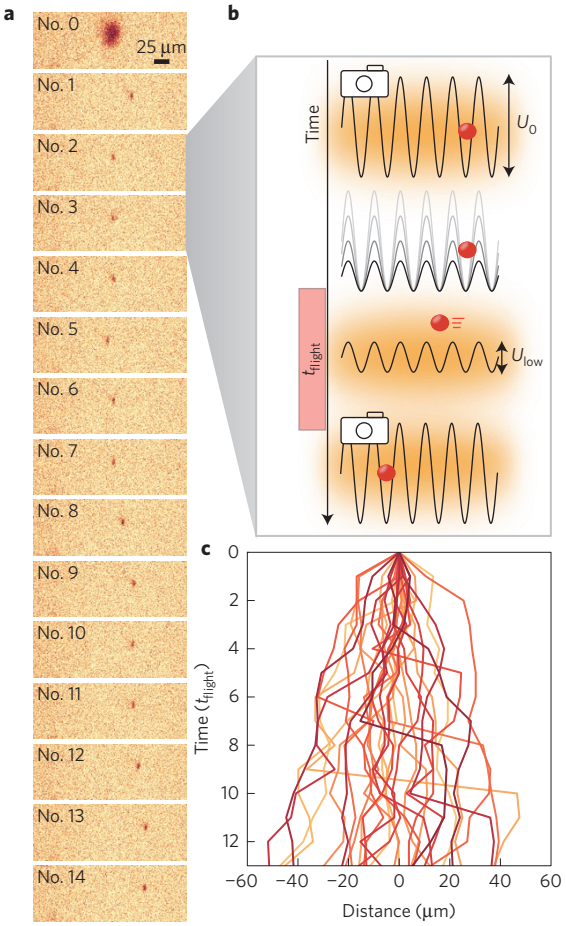

Figure 1 | Stroboscopic position imaging sequence. a, The atom number is first measured in the magneto-optical trap (image No. 0). The next 14 fluorescence images of a single atom are taken in the lattice and reveal its successive positions. **b**, After image acquisition, the light field intensity is reduced to zero and the lattice potential is adiabatically lowered to a value U_{low} to ensure thermal classical hopping for atoms with energies larger than the potential barrier. Diffusion is initiated by switching on the light field during a flight time t_{flight} between 0.1 ms and 50 ms. The lattice potential is then ramped up instantaneously before the next image to freeze the atom's position, before the whole process is repeated. **c**, A typical set of 30 single atom traces for $t_{flight} = 0.1$ ms.

atom to hop over the potential barrier; and, second, by illuminating the atom with near-resonant light to couple it to a quasi-thermal bath. Since the potential depth is always much higher than the atomic energy, quantum effects such as tunnelling are suppressed, resulting in classical dynamics. After a variable interaction time t_{flight}, we freeze the atomic motion by rapidly increasing the lattice depth to U_0 again. The atomic position is stroboscopically detected from high-resolution fluorescence images (Fig. 1a,b), before the potential depth is lowered for a next diffusion phase. We define the difference in position between two subsequent images as the flight distance. For each parameter set, we record approximately 600–1,000 traces consisting of 14 images. Taking an image involves scattering of approximately 10^6 photons off the tightly confined atom, so that all properties of the previous diffusion step are effectively reset and no memory on, for example, velocity or temperature is retained. As a result, the flights are independent of each other. During the longest measurements, the atom travels an average total distance of approximately 100 lattice sites, corresponding to a distance of approximately 40 μm. The stroboscopic imaging thus leads to a coarse graining of the atomic trajectory.

From the measured single atom trajectories (Fig. 1c), we determine the escape time from a potential well, the corresponding waiting distribution and the flight distance distribution (Fig. 2). The escape time τ_{esc} is the relevant time controlling diffusion between lattice wells. Its value may be obtained from the MSD, as diffusion only starts for $t_{flight} > \tau_{esc}$ (Fig. 2b). The distribution $\psi(\tau_w)$ of the waiting times τ_w between random hopping events is found to be exponential (Fig. 2a),

$$\psi(\tau_w) = \frac{1}{\tau_{esc}} e^{-\frac{\tau_w}{\tau_{esc}}} \quad (1)$$

We infer an escape time of $\tau_{esc} = 7$ ms by fitting an accumulated exponential function to the hopping probability (Fig. 2a). We further observe an exponential flight distance distribution $\phi(L)$ for short flight times (Fig. 2c),

$$\phi(L) = \frac{1}{2L_0} e^{-\frac{|L|}{L_0}} \quad (2)$$

with a characteristic length L_0. The distribution converges to a Gaussian in the limit of longer flight times (Fig. 2d and Supplementary Information), in agreement with the central-limit theorem. Even in the absence of a power-law tail distribution, this convergence is slow (non-exponential), as discussed below.

We may engineer the atomic motion by exploiting three independent mechanisms and their associated timescales. First, the interaction with the near-resonant light field leads to momentum diffusion with diffusion constant D_p (due to photon scattering) and damping at a rate γ (due to Doppler cooling)[29]; a steady state at temperature $k_B T_0 = D_p/\gamma$ is thus reached after a damping time $\tau_{damping} = \gamma^{-1}$. Second, the periodic potential adds the escape time τ_{esc} an atom needs to leave a potential well. Last, owing to the phase noise of the lattice (Supplementary Information), switching off the light field, while lowering the potential, leaves the atom in a non-equilibrium state at an increased temperature $T > T_0$ at the beginning of each flight of duration t_{flight}. In fact, the relevance of the non-equilibrium state for the dynamics can be adjusted by t_{flight}, as explained below. Each of the three times, $\tau_{damping}$, τ_{esc} and t_{flight}, may be changed independently, the first two by tuning the parameters of the light field and of the potential. In the present set-up, we fix $\tau_{damping} \simeq 1.3$ ms and $\tau_{esc} \simeq 7$ ms, and vary t_{flight} for simplicity.

We are able to explore diffusion over four decades of time (Fig. 3a) and change the diffusion coefficient, evaluated from a linear fit to the first ten data points of the MSD, by more than three orders of magnitude (two are shown in Fig. 3b). We identify four different regimes (Fig. 3): for $t_{flight} < \tau_{damping}$, the dynamics is dominated by the non-equilibrium phase-noise heating and the atom does not reach the steady state temperature T_0. As a result, the diffusion coefficient is greatly enhanced (grey and purple dots in Fig. 3b). For $t_{flight} > \tau_{damping}$, the atom is cooled to temperature T_0 and the motion is governed by the escape from the lattice wells (green and blue dots in Fig. 3b). For $t_{flight} \lesssim \tau_{esc}$, dynamics is induced mostly by single escape processes characterized by the exponential flight distance distribution in equation (2) (Fig. 2c). On the other hand, for $t_{flight} \gg \tau_{esc}$, each flight consists of several escape processes and the flight distance distribution approaches a Gaussian (Fig. 2d).

The motion of the atom is well described by an underdamped Langevin equation taking intra- and inter-well dynamics in the periodic potential into account (Methods). We obtain good agreement between the numerical simulations and the experimental data (Fig. 2c and d) without any free parameter. To obtain an analytical understanding of the diffusion process, we employ a continuous-time random-walk approach (CTRW)[6–8]. In this coarse-grained description, the details of the intra-well dynamics are neglected and the diffusion is modelled as a succession of hopping events of random length and occurring at random times. The

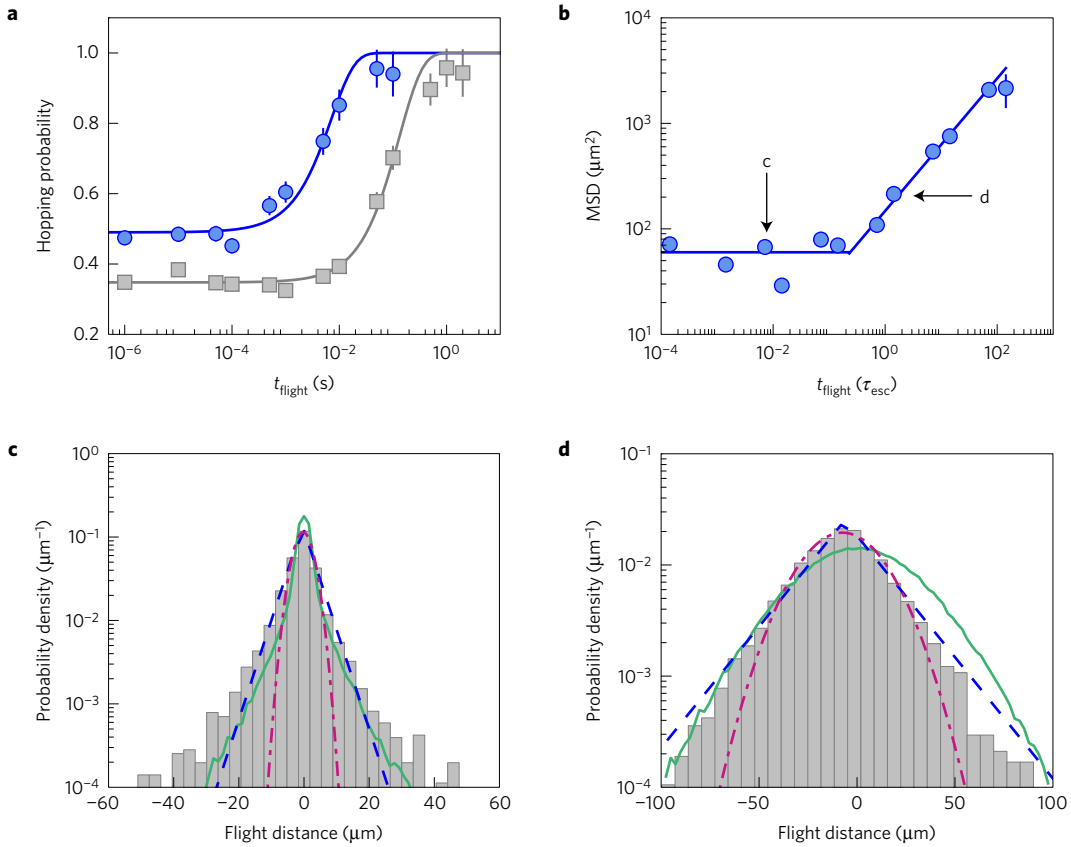

Figure 2 | Characteristic time and flight distances. a, Escape probability from a potential well versus the flight time t_{flight} for $U_{low} = 210\,\mu K \times k_B$ (blue circles) and $560\,\mu K \times k_B$ (grey squares). The solid lines are fits to a cumulative exponential distribution, equation (1), yielding the escape times $\tau_{esc} = 7$ ms and 131 ms, respectively. The non-zero probability for small t_{flight} is due to heating during the lowering of the potential. **b**, Mean-square displacement (MSD) versus t_{flight} for a single ramping process. Diffusion starts when $t_{flight} > \tau_{esc}$. The solid blue line is a double linear fit to the data points. Error bars in **a** and **b** represent standard statistical errors. **c**,**d**, Flight distance distributions for $t_{flight} = 0.1$ ms and $t_{flight} = 50$ ms, respectively, for $\tau_{esc} = 7$ ms. With increasing t_{flight} the flight distance distribution approaches a Gaussian according to the central-limit theorem. In both images the best fitting Gaussian is depicted (dashed-dotted line). The blue dashed line is a fit of the flight distance distribution $\phi(L)$, equation (2) (with $R^2 > 0.99$); the green solid line is the result of Langevin simulations.

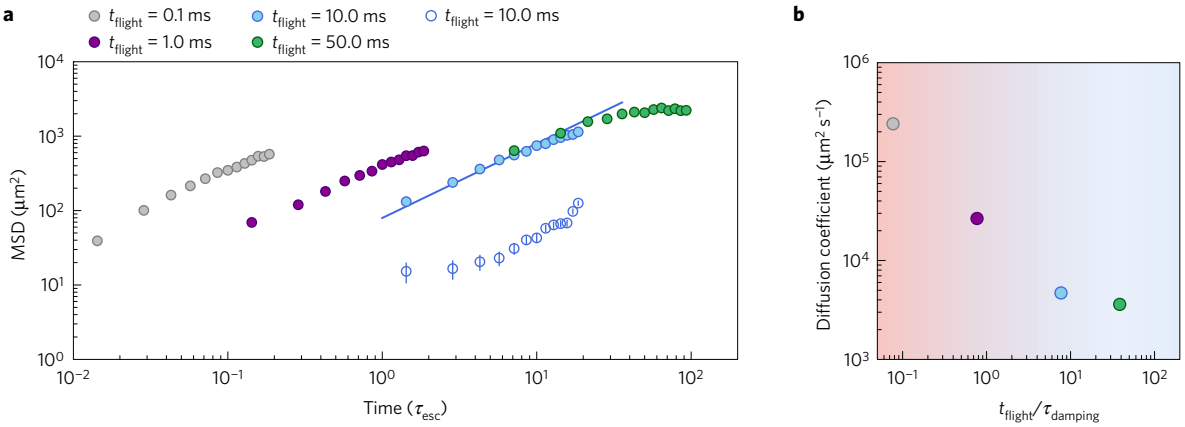

Figure 3 | Diffusion properties. a, Mean-square displacement (MSD) for different t_{flight} for a potential depth $U_{low} = 210\,\mu K \times k_B$. Open blue symbols are measured without a heat bath to confirm that diffusion is driven by the light field; they do not exhibit diffusive behaviour. The slight curvature of the green points at very long times reveals the effect of the axial confinement. The latter is completely negligible at shorter times. Error bars are evaluated from the standard deviation of the position and the statistical error. They are of the order of the symbol size. **b**, For $t_{flight} \lesssim \tau_{damping}$, the diffusion coefficient is enhanced owing to phase-noise heating of the lattice. For $t_{flight} \gtrsim \tau_{damping}$ diffusion is slowed down owing to effective cooling. The colour gradient depicts heating-dominated (red) and cooling-dominated (blue) regions.

corresponding waiting time and jump length distributions, $\psi(\tau_w)$ and $\phi(L)$, are chosen as the experimentally determined exponential distributions in equations (1) and (2). The CTRW model permits one to analytically predict nontrivial properties of the diffusion, such as the time evolution of the displacement distribution and higher-order correlation functions, in the cooling-dominated

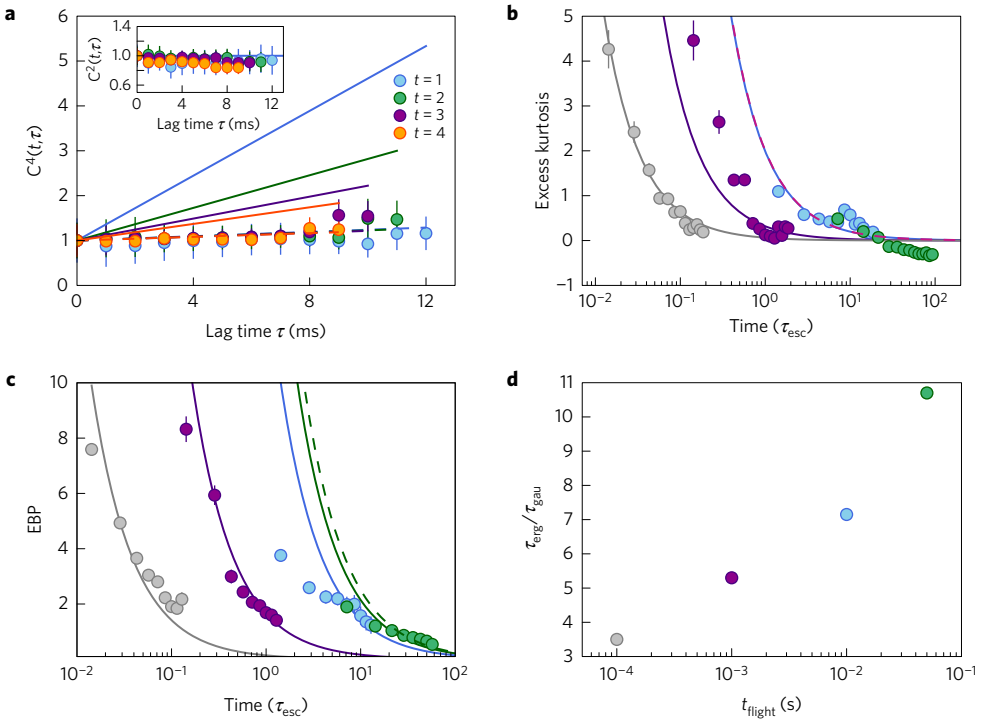

Figure 4 | Approach to Gaussianity and ergodicity. a, Two-point position correlation function $C^2(t,\tau)$, equation (4), (inset) and four-point correlation function $C^4(t,\tau)$, equation (5), for a flight time of $t_{flight} = 1$ ms. Different colours mark the time points in the trace. While $C^2(t,\tau)$ agrees with standard Brownian motion (given by the solid lines), $C^4(t,\tau)$ presents clear deviations. However, it agrees with the CTRW results, which are theoretical predictions without free parameters (represented by the dashed lines in all figures). **b**, The excess kurtosis $\kappa(t)$, equation (6), measured for the parameters of Fig. 2, decays as τ_{gau}/t, solid lines fit to the data points with $R^2 \geq 0.94$. **c**, The ergodicity breaking parameter EPB, equation (7), evaluated for the parameters of Fig. 2, decays as τ_{erg}/t (with $R^2 \geq 0.94$). **d**, The ratio τ_{erg}/τ_{gau} shows that ergodicity is established on a timescale similar to the Gaussianity in the non-equilibrium heating regime, $t_{flight} \leq \tau_{damping}$ (grey symbols), and on significantly longer timescales in the equilibrium regime, $t_{flight} > \tau_{damping}$. Error bars indicate the statistical error of Δx or x^2, respectively, and thus propagate by standard propagation of uncertainty.

regime $t_{flight} > \tau_{damping}$ (Methods and Supplementary Information). Specifically, the computed MSD,

$$\sigma^2(t) = \frac{2L_0^2}{\tau_{esc}} t \tag{3}$$

exhibits normal Brownian diffusion at all times. For our data, when fitting a power law $\sigma^2(t) \propto t^\alpha$ to the first ten data points, in analogy to the determination of the diffusion coefficient, we find $\alpha = 1.03 \pm 0.06$ (blue symbols in Fig. 3a) with $R^2 > 0.99$. In addition, the normalized two-point position correlation function[30] reads

$$C^2(t,\tau) = \frac{\langle \Delta x(t) \Delta x(t+\tau) \rangle}{\sigma^2(t)} = 1 \tag{4}$$

where τ is the time lag between two time points. Remarkably, this result is identical to that of standard Brownian motion[1]. Figure 4a shows good agreement with the experimental correlation function for all times t and time lags τ for $t_{flight} = 1$ ms. At the level of one-point and two-point correlation functions, both experiment and CTRW model thus appear to be undistinguishable from normal Brownian diffusion. The situation changes when considering the four-point correlation function,

$$C^4(t,\tau) = \frac{\langle \Delta x^2(t) \Delta x^2(t+\tau) \rangle}{\langle \Delta x^4(t) \rangle} = 1 + \frac{\tau}{3t + 6\tau_{esc}} \tag{5}$$

evaluated with two equal times. This quantity explicitly depends on the microscopic timescale τ_{esc} and differs from the Brownian motion result, which is recovered for $\tau_{esc} = 0$. Good agreement with the measured data is observed (Fig. 4a). To directly quantify the deviations from the displacement distribution from a Gaussian, we further calculate the excess kurtosis,

$$\kappa(t) = \frac{\langle \Delta x^4(t) \rangle}{3\langle \Delta x^2(t) \rangle^2} - 1 = \frac{\tau_{gau}}{t} \text{ with } \tau_{gau} = 2\tau_{esc} \tag{6}$$

Equation (6) vanishes for the Gaussian distribution of standard Brownian motion ($\tau_{esc} = 0$) and displays a slow, algebraic $1/t$ decay with a characteristic time τ_{esc} for the CTRW model. This expression confirms that τ_{esc} is the relevant time governing the convergence to the Gaussian central-limit result. The experimental data again nicely fit to the theoretical prediction (6) for $t_{flight} > \tau_{esc}$ (Fig. 4b). The overall excellent agreement between the coarse-grained experimental data determined via stroboscopic imaging and the coarse-grained CTRW model indicates that the latter provides an accurate effective description of the non-equilibrium dynamics of the atoms, akin to thermodynamics, which gives a correct coarse-grained description of equilibrium properties of a system.

To investigate the approach to ergodicity, we introduce the ergodicity breaking parameter (EBP)[28],

$$\mathrm{EBP}(t,\tau) = \frac{\langle \overline{x^2}(t,\tau)^2 \rangle - \langle \overline{x^2}(t,\tau) \rangle^2}{\langle \overline{x^2}(t,\tau) \rangle^2} \tag{7}$$

Here $\overline{x^2}$ denotes the time-averaged MSD with time lag τ—that is, the squared distance travelled in the interval τ, averaged over the entire trajectory of duration t (Methods). The EBP measures the degree of randomness of $\overline{x^2}$: it is zero for an ergodic system in the limit $t \to \infty$; at finite times, it quantifies how reliably the time average represents the ensemble average. For a particle diffusing

in a potential, the EBP generally decays as τ_{erg}/t, with a constant τ_{erg} that depends on the details of the system[31,32]. This behaviour is confirmed by our experimental data (Fig. 4c). While excess kurtosis (6) and EPB (7) exhibit the same slow $1/t$ decay, their convergence to zero depends crucially on the values of the two time constants, τ_{gau} and τ_{erg}. Figure 4d shows the ratio τ_{erg}/τ_{gau} of the two parameters obtained by fitting the respective experimental curves. We observe that τ_{gau} and τ_{erg} are of the same order in the heating-dominated non-equilibrium regime, $t_{flight} < \tau_{damping}$, where atoms are hotter than the heat bath. This situation is not described by the CTRW model. By contrast, in the equilibrium jump-process regime, $t_{flight} > \tau_{damping}$, where atoms have equilibrated with the heat bath, the constant τ_{erg} is much larger than τ_{gau}, indicating that ergodicity is here established on significantly longer timescales than Gaussianity. These findings show that Gaussianity and ergodicity may be approached on very different time constants in the same system, depending on the considered parameter regime.

Methods

Methods, including statements of data availability and any associated accession codes and references, are available in the online version of this paper.

Received 18 February 2016; accepted 6 September 2016; published online 10 October 2016

References

1. Risken, H. *The Fokker–Planck Equation* (Springer, 1989).
2. Fulde, P., Pietronero, L., Schneider, W. R. & Strässler, S. Problem of Brownian motion in a periodic potential. *Phys. Rev. Lett.* **35,** 1776–1779 (1975).
3. Barone, A. & Paterno, G. *Physics and Applications of the Josephson Effect* (Wiley, 1982).
4. Dorfman, J. R. *An Introduction to Chaos in Nonequilibrium Statistical Mechanics* (Cambridge Univ. Press, 1999).
5. Lutz, E. & Renzoni, F. Beyond Boltzmann–Gibbs statistical mechanics in optical lattices. *Nat. Phys.* **9,** 615–619 (2013).
6. Montroll, E. W. & Weiss, G. H. Random walks on lattices. II. *J. Math. Phys.* **6,** 167–181 (1965).
7. Klafter, J. & Sokolov, I. M. *First Steps in Random Walks* (Oxford Univ. Press, 2011).
8. Scher, H. & Lax, M. Stochastic transport in a disordered solid I. Theory. *Phys. Rev. B* **7,** 4491–4502 (1973).
9. Frey, E. & Kroy, K. Brownian motion: a paradigm of soft matter and biological physics. *Ann. Phys.* **14,** 20–50 (2005).
10. Kramers, H. A. Brownian motion in a field of force and the diffusion model of chemical reactions. *Physica* **7,** 284–304 (1940).
11. Wang, B., Anthony, S. M., Bae, S. C. & Granick, S. Anomalous yet Brownian. *Proc. Natl Acad. Sci. USA* **106,** 15160–15164 (2009).
12. Li, T., Kheifets, S., Medellin, D. & Raizen, M. G. Measurement of the instantaneous velocity of a Brownian particle. *Science* **328,** 1673–1675 (2010).
13. Han, Y. *et al*. Brownian motion of an ellipsoid. *Science* **314,** 626–630 (2006).
14. Fakhri, N., MacKintosh, F. C., Lounis, B., Cognet, L. & Pasquali, M. Brownian motion of stiff filaments in a crowded environment. *Science* **330,** 1804–1807 (2010).
15. D'Anna, G., Mayor, P., Barrat, A., Loreto, V. & Nori, F. Observing Brownian motion in vibration-fluidized granular matter. *Nature* **424,** 909–912 (2003).
16. La Porta, A., Voth, G. A., Crawford, A. M., Alexander, J. & Bodenschatz, E. Fluid particle accelerations in fully developed turbulence. *Nature* **409,** 1017–1019 (2001).
17. Wang, B., Kuo, J., Bae, S. C. & Granick, S. When Brownian diffusion is not Gaussian. *Nat. Mater.* **11,** 481–485 (2012).
18. Brokmann, X. *et al*. Statistical aging and non ergodicity in the fluorescence of single nanocrystals. *Phys. Rev. Lett.* **90,** 120601 (2003).
19. Jeon, J. H. *et al*. *In vivo* anomalous diffusion and weak ergodicity breaking of lipid granules. *Phys. Rev. Lett.* **106,** 048103 (2011).
20. He, Y., Burov, S., Metzler, R. & Barkai, E. Random time-scale invariant diffusion and transport coefficients,. *Phys. Rev. Lett.* **101,** 058101 (2008).
21. Manzo, C. *et al*. Weak ergodicity breaking of receptor motion in living cells stemming from random diffusivity. *Phys. Rev. X* **5,** 011021 (2015).
22. Lutz, E. Power-law tail distributions and nonergodicity. *Phys. Rev. Lett.* **93,** 190602 (2004).
23. Viterbi, A. J. & Omura, J. K. *Principles of Digital Communication and Coding* (Dover, 2013).
24. Sancho, J. M., Lacasta, A. M., Lindenberg, K., Sokolov, I. M. & Romero, A. H. Diffusion on a solid surface: anomalous is normal. *Phys. Rev. Lett.* **92,** 250601 (2004).
25. Sagi, Y., Brook, M., Almog, I. & Davidson, N. Observation of anomalous diffusion and fractional self-similarity in one dimension. *Phys. Rev. Lett.* **108,** 093002 (2012).
26. Douglas, P., Bergamini, S. & Renzoni, F. Tunable Tsallis distributions in dissipative optical lattices. *Phys. Rev. Lett.* **96,** 110601 (2006).
27. Katori, H., Schlipf, S. & Walther, H. Anomalous dynamics of a single ion in an optical lattice. *Phys. Rev. Lett.* **79,** 2221–2224 (1997).
28. Burov, S., Jeon, J.-H., Metzler, R. & Barkai, E. Single particle tracking in systems showing anomalous diffusion: the role of weak ergodicity breaking. *Phys. Chem. Chem. Phys.* **13,** 1800–1812 (2011).
29. Metcalf, H. J. & van der Straten, P. *Laser Cooling and Trapping* (Springer, 2002).
30. Risken, H. & Vollmer, H. D. Correlation functions for the diffusive motion of particles in a periodic potential. *Z. Phys. B* **31,** 209–216 (1978).
31. Deng, W. & Barkai, E. Ergodic properties of fractional Brownian–Langevin motion. *Phys. Rev. E* **79,** 011112 (2009).
32. Dechant, A., Lutz, E., Kessler, D. A. & Barkai, E. Fluctuations of time averages for Langevin dynamics in a binding force field. *Phys. Rev. Lett.* **107,** 240603 (2011).

Acknowledgements

This work was partially funded by the ERC Starting Grant No. 278208, the Collaborative Project TherMiQ (Grant Agreement 618074) and the SFB/TRR49. T.L. acknowledges funding by Carl Zeiss Stiftung. D.M. is a recipient of a DFG-fellowship through the Excellence Initiative by the Graduate School Materials Science in Mainz (GSC 266). F.S. acknowledges funding by the Studienstiftung des deutschen Volkes.

Author contributions

A.W. and F.K. conceived the experiment. F.K., M.H., T.L., D.M. and F.S. took experimental data, F.K. analysed the data. A.D. and E.L. developed the theoretical model and performed numerical simulations. All authors contributed in interpretation, discussion and writing of the manuscript.

Additional information

Supplementary information is available in the online version of the paper. Reprints and permissions information is available online at www.nature.com/reprints. Correspondence and requests for materials should be addressed to A.W.

Competing financial interests

The authors declare no competing financial interests.

Methods

Trapping and imaging single atoms. The caesium atoms are initially captured in a high-gradient ($\approx$250 G cm^{-1}) magneto-optical trap (MOT). On average, 0–5 atoms are loaded from the background gas and we postselect images where only one atom is present. Subsequently, we transfer the atoms to a combined optical trap, formed by a running wave optical dipole trap at $\lambda_{DT} = 1{,}064$ nm and an optical lattice. As a consequence, the atoms are radially confined by the running wave optical trap with a beam waist $w_{0,DT} = 22\,\mu$m and a power of 2.6 W, leading to a potential depth of $U_{0,DT} = 1$ mK. Axially the atoms are trapped within the sites of the lattice formed by two counter-propagating laser beams at $\lambda_{lat} = 790$ nm with a beam waist of $w_{0,Lat} = 29\,\mu$m and a maximum power of 650 mW per beam. During the experimental sequence, only the lattice potential is lowered, while the radial confinement is held constant at all times. This allows one to limit the diffusion of the atoms along the lattice axis and allows an effective one-dimensional description. The heat bath applied during the diffusion is engineered by the light field already used during the MOT phase. It consists of six counter-propagating orthogonal laser beams, red detuned with respect to the atomic resonance. In this light field the atoms are cooled by laser cooling, mainly Doppler cooling, while they constantly scatter photons[29].

We use the scattered photons (that is, fluorescence imaging) to precisely count the atom number during the MOT phase as well as to extract the position of the atoms in the lattice. An objective with a high numerical aperture (NA = 0.36) at a distance of 30.3 mm from the position of the atoms collects about 3.3% of the fluorescence photons. The collimated light is focused onto an EMCCD camera (Andor iXon 3 897) with a lens of focal length $f = 1{,}000$ mm, yielding a magnification of $M = 33$. Exposure times of 500 ms induce a signal-to-noise ratio of $\sim$5. The point spread function of the image system limits the position resolution to an uncertainty of 2 μm. For further details of our set-up we refer to ref. 33.

Error analysis. The uncertainty on the position of the atom is 2 μm, given by the finite optical resolution of the imaging system, and is thus about 5% for typical mean flight distances of 40 μm. The main source of errors is purely statistical and is of the order of 3–10% for the number of measured trajectories (600–1,000). The corresponding error bars are of the size of the symbols and thus not visible for most data points.

Control of the diffusion parameters. The diffusion is governed by three parameters: the diffusion constant D, the damping constant γ and the noise ξ. These quantities are directly related to the experimental parameters. The damping constant γ is given by the friction coefficient β/m_{Cs} of the light field (that is, molasses)[29],

$$\gamma = \beta/m_{Cs} = \hbar k^2 \frac{4 s_0 \delta/\Gamma}{m_{Cs}(1 + s_0 + (2\delta/\Gamma)^2)^2} \tag{8}$$

which is on the order of 5×10^3 s^{-1} for our parameters. Here δ is the detuning of the frequency of beams of the light field with respect to the atomic transition, Γ the natural line width of the caesium D2 line transition and $s_0 = I/I_s$ the saturation parameter given by the ratio of molasses intensity I over saturation intensity I_s. All of these parameters are precisely controlled in our system. The diffusion coefficient is $D = k_B T \gamma^{-1}$, where T is the atomic temperature, mainly set by the light field or by heating of the lattice due to phase noise. The random noise in the system is described by a Gaussian white noise ξ originating from individual, random photon scattering events at rate Γ_{scat}.

Langevin simulations. The observed dynamics of the atoms, in the absence of intentional heating periods, is theoretically well described by a Langevin equation for a single underdamped Brownian particle in a periodic potential,

$$\dot{p} = -\gamma p - U_{low} k \sin(2kx) + \sqrt{2D_p}\xi \tag{9}$$

Here, the first and last terms on the right-hand side are contributions due to illumination with the light field (that is, optical molasses). On the one hand, the red-detuning leads to cooling of the atoms and can be described as a classical damping term for a particle with mass m and damping coefficient γ, arising from the Doppler cooling force. On the other hand, random absorption and re-emission processes drive the microscopic motion, described by the momentum diffusion coefficient D_p and Gaussian white noise ξ. As a consequence, the light field acts as a reservoir of constant and adjustable temperature to which the atom is coupled. During the interaction with the light field the atom relaxes to a temperature determined by the molasses on timescales of the inverse cooling rate $\gamma^{-1} = 90$ ms. The second term on the right-hand side of equation (9) describes the periodic trap discussed above, with depth U_{low} and periodicity $d = \lambda/2 = k/(4\pi)$. The Langevin equation (10) is solved numerically by performing an Euler–Maruyama integration for 40,000 trajectories with 5×10^6 integration steps each.

Continuous-time random-walk model. We consider a CTRW model with waiting distribution $\psi(\tau_w)$ and jump length distribution $\phi(L)$, respectively given by the experimentally determined exponential functions (1) and (2). If up to time t, m jumps have occurred, the total displacement $x(t)$ is then the sum over the m corresponding jump lengths $L_{i=1,\ldots,m}$. The distribution of the total number of lattice sites traversed can accordingly be obtained in Fourier–Laplace space from the Montroll–Weiss equation[6],

$$\hat{\tilde{P}}(k,s) = \frac{1-\tilde{\psi}(s)}{s} \frac{1}{1-\tilde{\psi}(s)\hat{\phi}(k)} \tag{10}$$

where $\tilde{\psi}(s)$ is the Laplace transform of the waiting time distribution and $\hat{\phi}(k)$ is the (discrete) Fourier transform of the jump length distribution. These are given by

$$\tilde{\psi}(s) = \frac{1}{1+\tau_0 s} \quad \hat{\phi}(k) = \frac{1}{1+k^2 L_0^2} \tag{11}$$

The Laplace inversion is readily performed, and yields

$$\hat{P}(k,t) = \mathrm{e}^{-\frac{t}{\tau_0}[1-\phi(k)]} = \mathrm{e}^{-\frac{t}{\tau_0}\frac{k^2 L_0^2}{1+k^2 L_0^2}} \tag{12}$$

There does not seem to be a closed-form expression for the Fourier inversion. However, we may deduce several properties from the above expression. First, from the characteristic function equation (12), we can easily obtain the variance via differentiation as

$$\langle x^2(t)\rangle = \partial_k^2 \hat{P}(k,t)\big|_{k=0} = \frac{2L_0^2}{\tau_0} t \tag{13}$$

This corresponds to normal diffusion for all times, with a diffusion coefficient $D = L_0^2/\tau_0$. Second, for short times, $t \ll \tau_0$, we can expand equation (12) to lowest order to find

$$\hat{P}(k,t) \simeq 1 - \frac{k^2 L^2}{1+k^2 L^2} \frac{t}{\tau_0}$$

As a result, in position space we obtain

$$P(x,t) \simeq \delta(x)\left(1 - \frac{t}{\tau_0}\right) + \frac{t}{\tau_0}\frac{1}{2L_0} e^{-\frac{|x|}{L_0}} \tag{14}$$

For short times, the distribution of the displacement is thus given by an initial δ-peak that evolves into an exponential distribution equivalent to the jump length distribution. Note that the result for the variance (3) remains unchanged in the short-time approximation. On the other hand, for long times, $t \gg \tau_0$, the characteristic function equation (12) is exponentially small except for small $k \lesssim \sqrt{\tau_0/t}/L$, corresponding to $x \gtrsim \sqrt{t/\tau_0} L$. If x is not too large, we can accordingly perform a saddle-point approximation around $k = 0$ and find

$$\hat{P}(k,t) \simeq \mathrm{e}^{-\frac{t}{\tau_0} k^2 L_0^2} \tag{15}$$

The displacement distribution is thus a Gaussian,

$$P(x,t) \simeq \frac{1}{\sqrt{4\pi L_0^2 \frac{t}{\tau_0}}} \mathrm{e}^{-\frac{x^2}{4L_0^2 \frac{t}{\tau_0}}} \tag{16}$$

in this limit, as would be expected for the diffusive behaviour (3). However, we stress that this approximation breaks down at very large $x \gtrsim \sqrt{t/\tau_0} L$, where the exponential tails prevail. Nevertheless, the result for the variance (3) is valid exactly for all times, demonstrating that normal diffusion does not necessarily imply a Gaussian distribution.

Correlation functions of arbitrary order can also be obtained from the characteristic function (12). We find for instance, for the four-point correlation function,

$$C^4(t_1,t_2,t_3,t_4) = \frac{4L_0 t_1 (t_3 + 2t_2 + 6\tau_0)}{\tau_0^2} \tag{17}$$

To visualize the four-point correlation function, we restrict ourself to the case where two times are identical and normalize also by the fourth moment,

$$C^4(t,\tau) = \frac{\langle \Delta x^2(t) \Delta x^2(t+\tau)\rangle}{\langle \Delta x^4(t)\rangle} = 1 + \frac{\tau}{3t + 6\tau_0} \tag{18}$$

Ergodicity breaking parameter. The ergodicity breaking parameter is defined as[28,31]

$$\mathrm{EBP}(t,\tau) = \frac{\langle \overline{x^2}(t,\tau)^2\rangle - \langle \overline{x^2}(t,\tau)\rangle^2}{\langle \overline{x^2}(t,\tau)\rangle^2} \tag{19}$$

where the time-averaged mean-square displacement $\overline{x^2}$ is

$$\overline{x^2} = \frac{1}{t-\tau}\int_0^{t-\tau} \mathrm{d}t'(x(t'+\tau)-x(t'))^2 \tag{20}$$

The time lag τ is smaller than the absolute measurement time t. Physically, the EBP is the relative variance of the time-averaged MSD, which is a measure for the randomness of the latter. For large enough observation times and normal diffusion, the EBP tends to zero as the time-averaged MSD converges to the ensemble MSD for every single trajectory.

Data availability. The data that support the plots within this paper and other findings of this study are available from the corresponding author upon request.

References

33. Hohmann, M. *et al*. Neutral impurities in a Bose–Einstein condensate for simulation of the Fröhlich-polaron. *EPJ Quantum Technol.* **2,** 1–15 (2015).